A Laboratory X-ray Diffraction Based Instrument for Full field Stress-Strain Measurements in Metals

Ben Amir[1], Vatsa Gandhi[2], Angkur Shaikeea[3], Anthony Dennis[1], Haydn N. G. Wadley[4] and Vikram Sudhir Deshpande[1].

[1] Department of Engineering, University of Cambridge, Cambridge, CB2 1PZ, UK

[2] Department of Mechanical and Aerospace Engineering, University of California, Los Angeles, Los Angeles, CA, 90095, USA

[3] Graduate Aerospace Laboratories, California Institute of Technology, 1200 East California Boulevard, Pasadena, CA 91125, USA.

[4] Department of Materials Science and Engineering, University of Virginia

1 Abstract

Development of constitutive laws for elastic–plastic materials traditionally require hundreds of mechanical tests on statically determinate specimens to map their yield surface. Although accurate, this approach is slow and limits the pace of materials discovery, especially as modern alloy design and manufacturing accelerate while mechanical testing remains low throughput. Advanced processes such as additive manufacturing further complicate testing by producing non-uniform stress states even in nominally determinate specimens, making local mechanical response measurements essential, particularly under complex stress state incurred in most engineering applications. Digital Image Correlation (DIC) provides full-field total strain measurements and is valuable for elastic characterisation, but it cannot capture the plastic deformation fields needed to resolve history-dependent plasticity. In other words, understanding plastic behaviour requires access to an internal (history) variable beyond total strain. In this work, we address this longstanding gap by introducing a new laboratory instrument based on Energy-Dispersive X-ray Diffraction (EDXRD) that enables full field measurement of elastic strain field concurrently with DIC based full field strains to regularize the problem of constitutive modelling in metals. Consequently, we can extract local stress-strain responses along diverse loading paths (multi-axial stress states) within a single specimen, yielding dozens of independent measurements from a single test. This capability opens the door to using complex specimens (statically indeterminate) that intentionally generate a wide range of strain paths, allowing the yield surface and its evolution to be characterised from only a few experiments.

2 Introduction

In recent decades, the advent of modern synchrotron radiation sources has fundamentally transformed materials science, enabling researchers to probe the structure and behavior of materials under dynamic conditions with unprecedented clarity. These powerful facilities provide extremely bright, high-energy X-ray beams that allow for the in-situ and operando characterization of materials, offering direct observational windows into processes as they occur within complex environments (Hemley et al., 2005; Mino et al., 2018; Stan et al., 2018). This capability has moved many areas of materials research from a paradigm of post-mortem inference to one of direct, real-time observation, accelerating the development of advanced structural, functional, and energy-related materials (Bulavchenko & Vinokurov, 2023).

A preeminent example of a technique that has flourished in the synchrotron environment is Energy Dispersive X-ray Diffraction (EDXRD). In contrast to conventional Angle Dispersive X-ray Diffraction (ADXRD), which uses a monochromatic beam and a scanning goniometer, the EDXRD method employs a polychromatic X-ray beam at a fixed scattering angle, 2θ. A complete diffraction pattern is collected simultaneously by an energy-sensitive point detector, where the energy (E) of a diffracted photon is related to the material's lattice spacing (d_{hkl}) by the Bragg condition, expressed as $E = hc/(2d_{hkl}sin\theta)$ (Chen et al., 2018; Greenberg & Iniewski, 2018). This fixed-geometry with high efficiency point detector offers distinct advantages, particularly its accuracy for measurement of lattice strains averaged over grains pointwise in a specimen (Withers & Bhadeshia, 2001). They are also suitable for experiments in constrained sample environments, such as high-pressure cells or electrochemical devices, which require only small, fixed optical access windows (Chen et al., 2018). Whereas, ADXRD requires large 2D detectors with finer pixel size and involves solving an inverse problem to reconstruct lattice strains in 3D (Poulsen et al., 2001). We realized that when the interest is in average strains over a collection of grains in specific directions (the idea for measurement of continuum strains), EDXRD is a more practical method. Long gauge volumes along the beam direction limit the 3D spatial resolution which is not of interest in this work.

In engineering, predicting the fatigue life and ensuring the structural integrity of components is critical. Synchrotron EDXRD is a key technology in this domain, offering non-destructive, 2D mapping of residual stress fields (averaged through the thickness of the specimen along the beam direction) like a full field measurement. This is particularly valuable for analyzing components subjected to processes like welding and shot peening, where internal stresses can significantly impact performance and longevity (Mäde et al., 2024; Zhang et al., 2020). Beyond these practical applications, EDXRD provides a crucial bridge to theoretical science, especially in the field of continuum mechanics (Daymond, 2004). While models such as the Finite Element (FE) method can predict a continuum elastic strain, these theoretical predictions demand experimental validation. EDXRD supplies this validation by directly measuring lattice strains, which are then used to calculate a macroscopic equivalent elastic strain for direct comparison with the models. This synergy makes EDXRD an indispensable tool for investigating complex phenomena, such as strain localization by measuring lattice strains. While there have been attempts to use such lattice level strains to refine complex theoretical frameworks in plasticity (Croft et al., 2008), there is a paucity of literature on measurement of continuum properties that can be used to learn constitutive behaviour in plasticity. One reason is that despite the widespread application of EDXRD, it is constrained by its reliance on large-scale synchrotron facilities. The limited availability of beamtime is often incompatible with the iterative nature of fundamental research and rapid industrial development cycles. Consequently, there is a critical need to translate these high-energy diffraction capabilities to the laboratory scale to accelerate scientific progress.

The translation of advanced characterization techniques from large-scale synchrotron facilities to the standard laboratory has a history of catalysing scientific progress by making powerful tools more accessible. A pertinent example is Diffraction Contrast Tomography (DCT), which, after its development at synchrotrons, was adapted into a laboratory-scale version (LabDCT) that is now widely used for 3D grain mapping(Ludwig et al., 2009). Similarly, Small-Angle X-ray Scattering (SAXS), initially refined at synchrotron facilities, has become a routine and powerful laboratory tool thanks to improvements in X-ray optics and detectors, significantly enhancing its research impact (Jeffries et al., 2021; Stuhrmann, 1989). The most recent innovation following this crucial path of technological democratization is three-dimensional X-ray diffraction (3DXRD), which has only recently been demonstrated on a laboratory scale (Oh et al., 2025).

In this work, we directly address the critical gap between traditional constitutive model calibration and real-world, multi-axial stress states. We follow the established path of technological translation by developing a laboratory-scale EDXRD system, designed specifically for advanced in-situ materials characterization. This advance is made possible by the convergence of high-power laboratory X-ray sources (rotating anode and most recently MetalJet technology) capable of producing sufficient polychromatic flux and high-performance energy-sensitive detectors used in this study. We present this system's utility by benchmarking its measurements against the data required to validate traditional continuum plasticity models, such as J2 plasticity. This approach provides a direct challenge to conventional calibration (which relies on homogeneous, uniaxial tests), by providing direct, localized measurements of the internal strain field under the heterogeneous stress conditions found in real-world components.

Finally, we discuss the outlook for this Lab-EDXRD methodology. Beyond its core application of providing rich, multi-axial validation data, it can also supplement the growing synchrotron user base by enabling feasibility studies and long-duration experiments. By overcoming the accessibility bottleneck, laboratory-based EDXRD has the potential to become a mainstream tool for materials research, industrial quality control, and education, significantly accelerating the pace of innovation.

3 Results and Discussion

3.1 Construction of the lab scale instrument

The development of a laboratory-scale EDXRD system is not a direct translation of synchrotron facilities due to fundamental differences in source characteristics; notably, laboratory X-ray sources are inherently polychromatic, divergent, non-coherent, and typically limited by significantly lower photon flux. However, for applications in continuum mechanics, the primary objective is to measure the macroscopic continuum strain rather than resolve intra-granular features. This is achieved by interrogating a gauge volume large enough to contain thousands of randomly oriented grains. By collecting the diffraction signal from this ensemble, the system provides a statistically representative average of the lattice deformations, effectively smoothing out the discrete nature of the microstructure to yield continuum-level elastic properties.

The integrated experimental setup is designed to perform these measurements in-situ under mechanical load. The system comprises a high-brightness MetalJet X-ray source (Excillum E1+). Unlike conventional solid-anode sources restricted by thermal limits, this source utilizes a regenerative liquid-metal anode to enable a high electron beam power of 1000W, which generates a high-flux polychromatic beam (10-160 keV). This divergent beam (20 degree cone angle) is shaped by a specialized optics before illuminating the specimen, which is mounted within a custom-built loading rig.

As the principle of operation relies on EDXRD, unlike monochromatic angle-dispersive methods, the detector angle 2θ is fixed, and the diffraction condition is satisfied for various interplanar lattice planes with perpendicular distances d_{hkl} represented by Miller indices (hkl). The diffracted photon energies (E) is then expressed according to Bragg's Law as:

$$E = \frac{hc}{2\mathrm{d}_{\mathrm{hkl}} \sin\theta} \qquad \text{Eq 1}$$

where h is Planck's constant and c is the speed of light.

To resolve the orthogonal components of the elastic strain tensor, the system utilizes two High Purity Germanium (HPGe) detectors. A critical feature of the alignment is the orientation of the loading frame, which is tilted by 5° relative to the incident beam. This specific geometry ensures that the scattering vectors collected by the detectors correspond precisely to the longitudinal (ε_{yy}) and transverse (ε_{xx}) axes of the specimen.

Complementing the internal elastic strain measurements, the system is equipped with a stereo Digital Image Correlation (DIC) setup. This optical system maps the full-field total surface strain, allowing for the simultaneous decomposition of elastic and plastic deformation components. A global extensometer and load cell provide secondary verification of the boundary conditions. Detailed specifications regarding the MetalJet source, Collimation, HPGe detectors, and the precise alignment procedure are provided in the subsequent sections.

3.1.1 X-ray source: MetalJet technology

The experimental setup utilizes an Excillum MetalJet E1+ (Excillum, Sweden) X-ray source, which employs a liquid-metal-jet anode. The anode target consists of a molten gallium-based alloy (ExAlloy-I2) that is maintained in a fluid state by integrated heating elements. For the experiments, the source was operated at its maximum acceleration voltage of 160 kV and an emission current of 6.5 mA, resulting in a total electron beam power of 1000 W. This configuration produces a nominal 30 µm round X-ray focal spot and generates a conical high-flux (cone angle ~ 20 degrees), polychromatic X-ray spectrum with energies ranging up to 160 keV.

3.1.2 Broadband collimation of X-rays (20-60 keV)

We employ broadband collimation of hard X-rays using high-precision Montel mirrors (ASTIX-f-115/885-L100-HE), specifically designed and manufactured by AXO Dresden, Germany for the MetalJet E1+ ExAlloy I2 system (160 kV, 1kW). The mirror system comprises two orthogonally arranged, highly polished, multilayer coated Si mirrors mounted at 90° to each other, forming an L-shaped configuration. Each mirror in the Montel assembly reflects the X-ray beam along one spatial direction: one provides horizontal deflection, while the other provides vertical deflection. Together, they enable two-dimensional beam shaping by collimating and focusing the X-rays, depending on the mirror curvature and coating design. In our case, the multilayer coatings are fabricated to Standard Curvature Accuracy (SCA) and are optimised for operation within the 20–60 keV bremsstrahlung energy range up to 1kW. The Montel mirrors effectively transform the divergent X-rays (cone angle ~20°) from the source into a parallel beam with a divergence of $\sim 0.4\ mrad$ across the specified energy range. The mirrors are 100 mm in length, with a primary focal distance (the distance between the thermal spot of the X-ray source and the mirror centre) of $f_1 = 115\ mm$, and a secondary focal distance (from the mirror centre to the focal spot) of $f_2 = 885\ mm$. For a 30 μm source size from the MetalJet E1+, the resulting focal spot has a FWHM of 400 μm and an estimated photon count of ~2e7 ph/s (ignoring In-K and Sn-K characteristic radiation).

The mirrors are housed (UMH150) within a water-cooled enclosure, which maintains a stable operating temperature of ~ 22°C. A beryllium window is provided at the entrance side and a Kapton window at the exit side. The housing is connected to the MetalJet exit window via a 4 mm thick tungsten adaptor, which serves to contain scattered X-rays from the source. For positional alignment, the housing is mounted on a two-axis translation stage, allowing movement along the X and Y axes to align the mirrors precisely with the MetalJet beam. The collimator produces four beam paths orthogonal: two singly reflected beams, one direct (unreflected) beam, and one doubly reflected (collimated) beam.

The performance of the collimating optics was quantified, and the results are presented in Figure 1. The graph compares the photon counts measured by the detector (placed at 2000 mm from the exit window of the source) during a 1-second exposure for two configurations: with and without the collimator installed. For both measurements, the beam was passed through the 300 µm pinholes located at the base of a brass blades. These pinholes serve a dual purpose: they facilitate the precise alignment of the X-ray beam and isolate the doubly-reflected beam from the optics for use in the experiment.

The baseline measurement without the collimator shows a uniform signal of about 300 photon counts. In contrast, the focused beam from the collimator produces a peaked intensity profile with a peak of about 1600 photon counts. This represents more than a five-fold increase in peak flux, highlighting the collimator's critical role in delivering a high-intensity beam to the specimen.

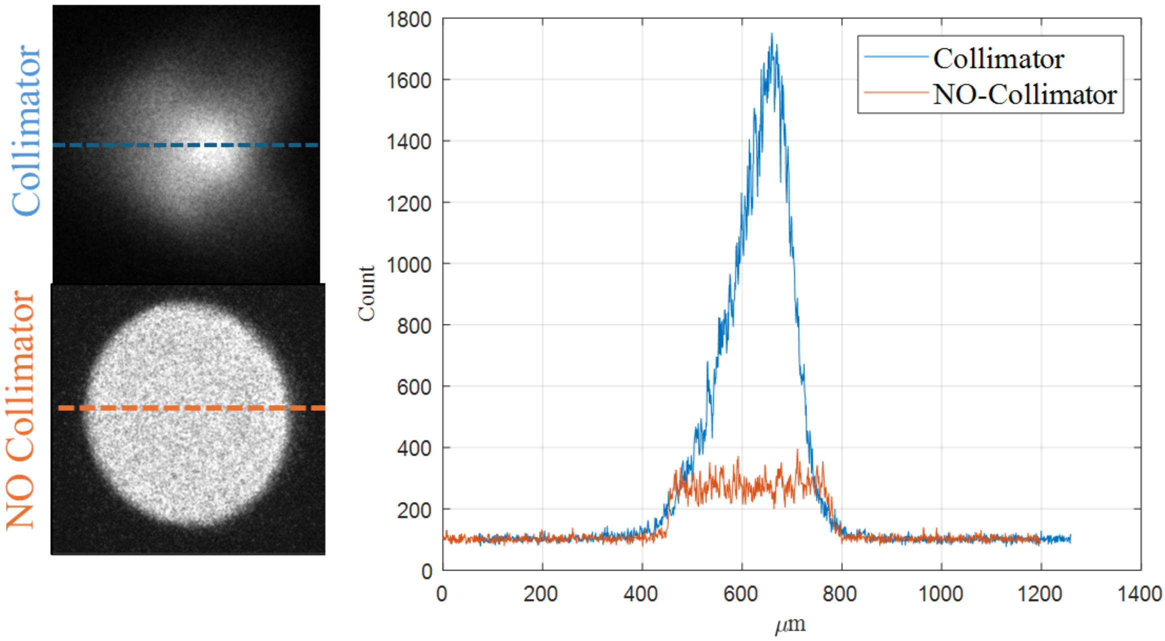

Figure 1 A comparison of the X-ray flux measured through a 300 µm pinhole for a 1-second exposure. The orange line shows the baseline flux without the collimator (~300 counts), while the blue line shows the focused beam with the collimator, peaking at ~1600 counts.

3.1.3 High Purity Germanium (HPGe)

EDXRD spectra are obtained using Broad Energy Germanium Detectors (BEGe™) from Mirion (10 mm thick 99% pure Germanium single crystal with a diameter of 16 mm) housed in vacuum and cooled by a compact CP5 cooler (model: EGX 25-20-ER type P). These are high efficiency (>90 % energies <100 keV) with energy resolution of ~300 eV for energies below 100 keV that count single photons and the energy of the photon, producing a spectrum of counts and energy. The energy range in each detector is calibrated using a known radioactive source. Americium-241, an isotope of Am which is an alpha source with a decay energy of 59.54 keV. Settings used were: number of channels 1024, energy range 0 – 80 keV, corresponding to an interval size of 78 eV.

3.1.4 Digital Image Correlation (DIC) Setup and Analysis

Concurrent to the elastic strain measurements from the EDXRD setup, the full-field surface displacements and total strains were measured using a three-dimensional (3D) stereo Digital Image Correlation (DIC) system from Correlated Solutions. The setup consisted of two Sony IMX540, 1.2" CMOS, 12 MP cameras, each equipped with 50 mm lenses, positioned at a stereo angle of approximately 20°. The specimen was illuminated with a single diffused, high-intensity LED lights to ensure uniform, non-glare lighting. Prior to testing, a stochastic speckle pattern was applied to the specimen surface using a matte white base coat followed by a fine mist of black paint.

The system was calibrated using a standard calibration target. Images were acquired at a resolution of 1920 x 1080 pixels (Full HD), with the region of interest (ROI) on the specimen occupying approximately 50% of the field of view. The images were processed using the Vic-3D software. A square subset (grid) size of 35 x 35 pixels was used, with a step size of 7 pixels. The Green-Lagrange strain tensor was calculated from the displacement data using a virtual strain gauge filter size of 15.

3.1.5 Alignment Setup

The experimental alignment is defined with respect to a right-hand coordinate system, as depicted in Figure 2. The Z-axis is aligned with the incident, collimated X-ray beam, and the Y-axis is oriented vertically, parallel to the tensile loading direction. The specimen, mounted in the custom loading frame, was positioned at the gauge volume (GV), where the diffracted beams intersect with the incident beam.

Two HPGe detectors were positioned to capture the diffracted X-rays at a fixed scattering angle of $2\theta = 10^{\circ}$, The vertical detector (HPGeV) was positioned in the Y-Z plane, while the horizontal detector (HPGeH) was positioned in the X-Z plane. In energy-dispersive diffraction, the measured lattice spacing ,d, corresponds to the crystal planes perpendicular to the scattering vector, q, which bisects the angle between the incident and diffracted beams. Therefore, for a diffraction angle of $2\theta = 10^{o}$, the vector q is inclined by $\theta = 5^{\circ}$, relative to the direction perpendicular to the incident beam. To ensure that the measured lattice strains correspond precisely to the principal sample axes, the entire loading frame was tilted by 5° around the X-axis. This alignment ensures that the scattering vector for the vertical detector (qV) is parallel to the specimen's tensile loading direction (YY). Similarly, the horizontal detector was arranged to measure the strain component in the transverse direction (XX). Each diffracted beam was further restricted by a pair of receiving slits to ensure precise gauge volume definition before reaching the detectors.

Concurrently, a stereo- DIC system was positioned to monitor the specimen's surface for full-field strain mapping, complemented by an extensometer for global strain measurement, while the applied force was monitored using a 10 kN load cell (Omega Engineering, UK).

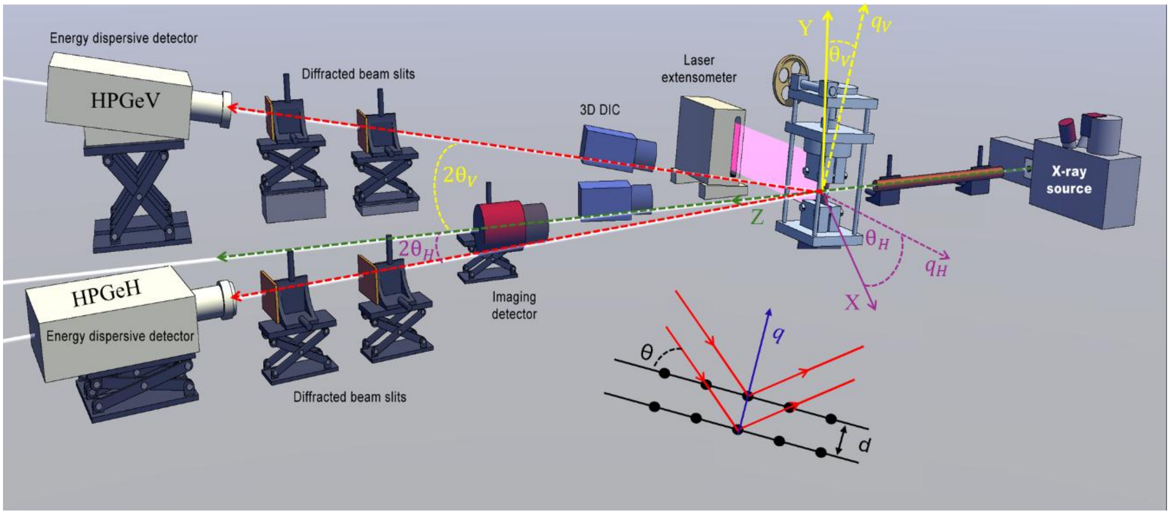

Figure 2: Schematic of the in-situ experimental setup for combined XRD and DIC measurements. A collimated X-ray beam illuminates the specimen, which is held in a loading frame tilted at 5° to the incident beam. Two area detectors are positioned to capture the transmitted diffracted X-rays, enabling the measurement of lattice strains in the loading (Y) and transverse (X) directions.

4 Experimental Methods

4.1 Material and Specimen Design

The material investigated in this study was Ti-6Al-4V (Ti64), sourced from Goodfellow, UK as a 0.5 mm thick as-received plate. Two distinct specimen geometries were cut from the plate via Electrical Discharge Machining (EDM). First, for initial validation and constitutive model calibration, standard "dog-bone" shaped tensile specimens were used, conforming to the ASTM E8 standard. Second, to investigate behavior under complex, multiaxial stress states, a double-notched plate specimen was designed. This notched configuration was specifically chosen to create a wide range of stress combinations, as detailed by (Shishvan & Deshpande, 2025) . The geometry of both the dog-bone and notched specimen types is detailed in Figure 3(A) and (B).

Figure 3 C depicts microstructure of the alloy as examined by optical microscopy, scanning electron microscopy (SEM) and electron backscatter diffraction (EBSD) to determine the grain structure of the as received material.

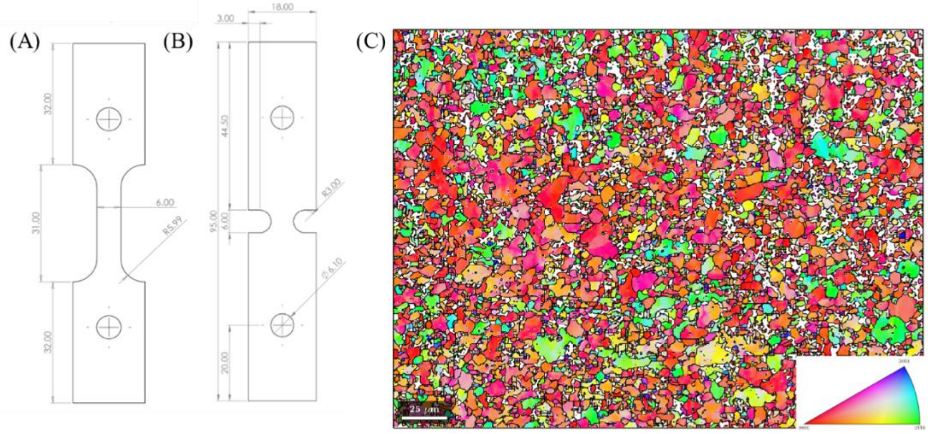

Figure 3 Specimen geometries and as-received material microstructures. ***(A)*** *The "dog-bone" uniaxial tensile specimen (ASTM E8).* ***(B)*** *The double-notched plate specimen, designed to create a wide range of stress states.* ***(C)*** *EBSD Inverse Pole Figure (IPF) map colored according to the loading direction, revealing the grain orientation and morphology.of the Ti-6Al-4V alloy.*

As described in the previous section, the incident x-ray beam is 300 microns in diameter, and in our specimen the grains are of average size ~5 microns which implies we have thousands of grains that we are measuring within the gauge volume which is define as 300 μm in diameter and 500 μm in thickness.

4.2 Loading and Data Acquisition Protocol:

A stepwise displacement control loading protocol was implemented. The specimen was loaded incrementally to predefined load levels. At each step, the macroscopic displacement was held constant for the duration of the data acquisition sequence, which included the collection of both diffraction patterns and a set of stereo images for DIC.

The data acquisition began with a comprehensive scan of the region of interest (ROI) in the specimen's initial, pristine state to establish a stress-free reference (d_0). Following this, the specimen was loaded to the first of the stepwise load level. At this constant displacement, a raster scan was performed across the measurement grid, with the x-ray beam dwelling at each spatial point for 200 seconds to acquire a high-quality energy-dispersive diffraction spectrum. This entire process was repeated for each subsequent load step.

For each acquired spectrum, the diffraction peaks were individually fitted with a Gaussian function. This fitting procedure precisely determines the peak's key parameters: its center position (mean), amplitude, and width (characterized by the Full Width at Half Maximum, FWHM). The elastic strain of the lattice (ε_{yy}^{e} and ε_{xx}^{e}) was then calculated from the relative shift in the peaks centre position with respect to its average position in the pristine reference state. This peak-fitting and strain calculation procedure is illustrated schematically in Figure 4.

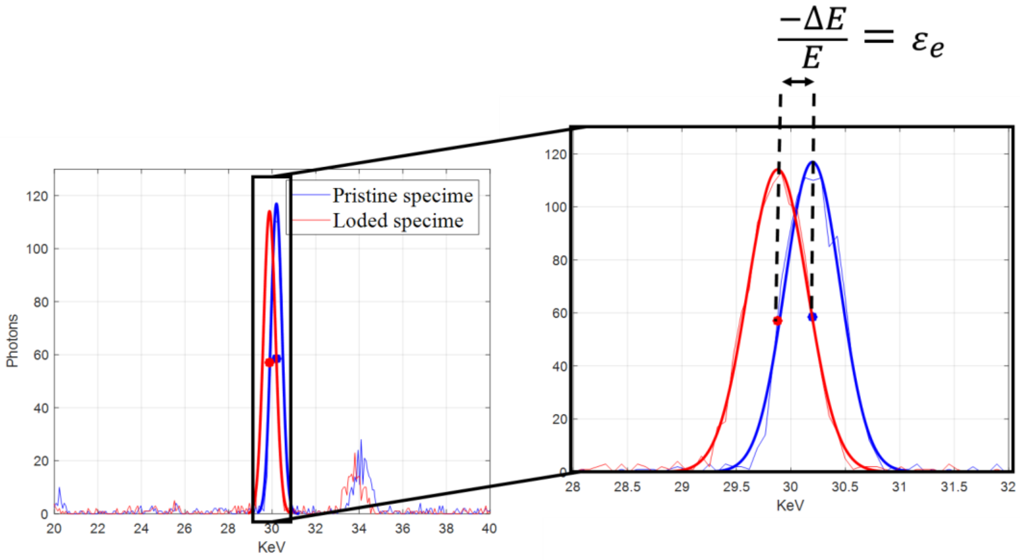

Figure 4 Schematic of the strain calculation procedure from a single diffraction peak. The center position of a peak in a loaded state is compared to its reference position in the pristine (unloaded) state to determine the lattice strain.

4.3 Adjustments for Stress Relaxation behavior in Ti-6Al-4V

The selected Ti-6Al-4V alloy is known to exhibit time-dependent stress relaxation at room temperature. To ensure that all measurements were conducted under a constant load while the macroscopic displacement is held fixed, a specific hold protocol was implemented at each step of the loading sequence. After reaching a predefined displacement level, the specimen's global displacement was held constant for 25 minutes prior to the start of the DIC and XRD data acquisition sequence. This hold period allowed for the initial, more rapid stress relaxation to subside, ensuring that measurements were taken in a state where the relaxation rate had become minimal and approximately linear. To characterize and validate this protocol, dedicated relaxation tests were performed on the notched specimen. Figure 5 A shows the evolution of the global reaction force as a function of time, during two such hold periods: one at the onset of global plasticity and another at the maximum applied load. As observed in both cases, the rate of force decay diminishes significantly and approaches a linear trend after approximately 20 minutes (Figure 5 A). This confirms that the 25-minute hold time was sufficient to achieve a near-equilibrium state for measurement. This same hold protocol was applied during the tests on the uniaxial specimens for consistency, although the magnitude of the observed relaxation was less pronounced in the uniform stress state.

In addition to characterizing the material's time-dependent behaviour, the directional dependence of its mechanical properties was investigated to assess the degree of plastic anisotropy. Standard uniaxial tensile tests were conducted on two "dog-bone" specimens as detailed above in Figure 3 A. Both specimens were machined via EDM from the as-received Ti-6Al-4V sheet but at two orthogonal orientations: one parallel to the sheet's primary rolling direction (termed the 'normal orientation') and a second at 90° to this direction (termed the 'perpendicular orientation'). The tests were performed at a constant strain rate of 2.5×10^{-3} s^{-1}, corresponding to quasi-static loading conditions. Figure 5 B presents the resulting engineering stress-strain curves for both orientations. The response of the specimen aligned with the normal orientation, which was used for all subsequent EDXRD experiments, is shown in red. The response of the perpendicular specimen is shown in black. A high degree of overlap is evident between the two curves throughout the entire elastic regime and the plastic strain exhibits very similar behaviour up to 2.5% strain.

This excellent agreement indicates that the as-received material possesses a high degree of in-plane isotropy. Although the out-of-plane properties were not explicitly characterized, these findings support the adoption of an isotropic constitutive framework (i.e., Isotropic Hooke's Law and J2 Plasticity) as a reasonable approximation for the subsequent analysis of the experimental data.

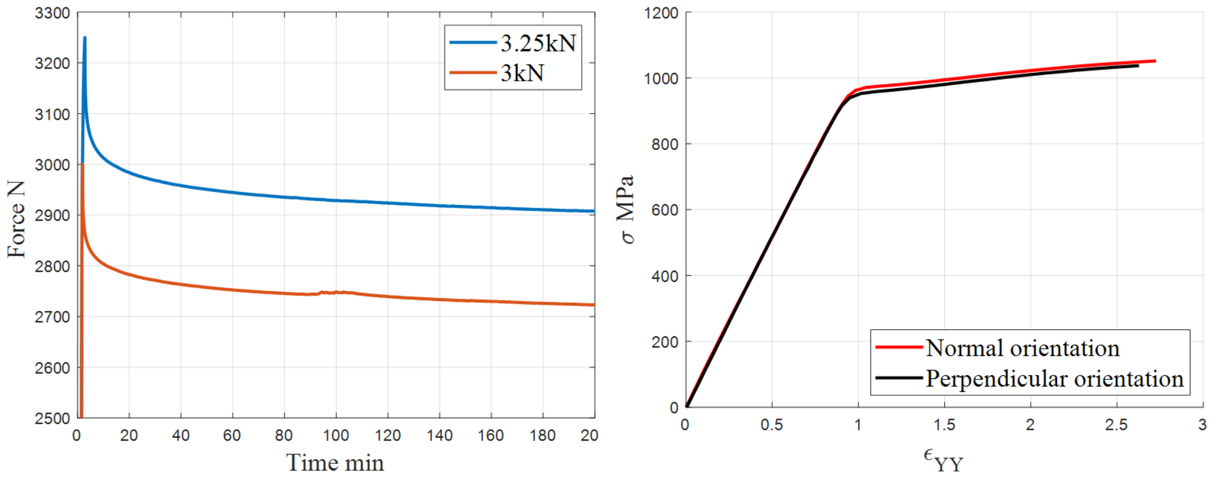

Figure 5 Material characterization and experimental protocol validation. (A) Stress relaxation behavior of the notched Ti-6Al-4V specimen, showing the global force decay over time during fixed-displacement holds. The relaxation rate becomes minimal after ~20 minutes, validating the 25-minute hold time used for measurements. (B) Verification of material isotropy, showing overlapping engineering stress-strain curves for specimens machined parallel (red) and perpendicular (black) to the rolling direction. The agreement confirms the material's isotropic behavior. Stress in MPa and strain in %.

4.4 Finite Element Analysis

To provide a numerical benchmark for the experimental results, plane-stress finite element (FE) analysis was performed using MOOSE (Permann et al., 2020). The geometry of the FE model replicated the double-notched specimen detailed in Figure 3. The model was meshed with 1796 second-order plane-stress elements with reduced integration. The mesh was significantly refined in the region of the notch root to accurately capture the high stress and strain gradients expected in this area.

The material behaviour was described by a rate-independent, elasto-plastic constitutive model. The total small-strain tensor (ε) was additively decomposed into its elastic (ε^e) and plastic (ε^p) parts as:

$$\varepsilon = \frac{1}{2}\left(\nabla u + \nabla u^T\right) = \varepsilon^e + \varepsilon^p$$

Eq 2

The elastic response was modelled as linear and isotropic, governed by Hooke's Law as follows:

$$\sigma = C{:}\,\varepsilon^{e};\ C_{ijkl} = \lambda\delta_{ij}\delta_{kl} + \mu\left(\delta_{ik}\delta_{jl} + \delta_{il}\delta_{jk}\right) \tag{Eq 3}$$

Plasticity was modelled using a standard J2 flow theory with an isotropic, power-law hardening rule, where the yield stress (σ_y) evolves with the equivalent ε^p according to:

$$\sigma_y(\varepsilon^p) = \sigma_{y0}\left(1 + \left(\frac{\varepsilon^p}{\varepsilon_0}\right)^N\right) \tag{Eq 4}$$

Mechanical equilibrium was implemented as follows:

$$\nabla \cdot \sigma = 0$$

The boundary conditions were chosen to replicate the experiment: the bottom surface of the model was constrained against displacement in the loading direction (Y-axis), and a force-controlled load was applied to the top surface to match the experimental loading points.

All material parameters required for the constitutive model were determined directly from the experimental stress-strain data of the uniaxial "dog-bone" specimen test, presented in Figure 5. The elastic constants were extracted from the initial linear portion of this curve, yielding a Young's Modulus of E = 115 GPa and a Poisson's ratio of $\nu = 0.35$. The plastic parameters for the power-law hardening model were then calibrated by fitting the model's prediction to the post-yield data from the same experiment. This calibration resulted in an initial yield stress of σ_{y0}= 1000 MPa, hardening exponent of N=0.8 and $\varepsilon_0 = 0.5$, All experimentally determined parameters are consistent with values reported in the literature for Ti-6Al-4V.

5 Methodology Validation

5.1 Uniaxial Response and Strain Decomposition:

The primary validation of the dual-measurement technique was conducted by comparing the strain evolution measured by DIC and EDXRD during a standard uniaxial tensile test. Figure 6 plots the measured strain components as a function of the globally applied stress. The total strain (measured by DIC) is represented by dashed lines, while the elastic lattice strain (measured by EDXRD) is shown by solid lines. The components in the axial loading direction (ε_{yy}) are colored blue, and the components in the transverse direction (ε_{xx}) are colored orange.

Two distinct regimes are evident. In the initial elastic loading region, there is excellent agreement between the total and elastic strain measurements from both the axial and transverse directions. This strong correspondence serves as a critical cross-validation, confirming that both independent measurement systems are accurately capturing the material's response in the elastic domain.

Upon reaching the yield point, as would be expected, a clear divergence between the total and elastic strain curves is observed. As the material begins to deform plastically, the total axial strain increases non-linearly. In contrast, both the axial and transverse elastic strain components (solid lines) maintain their linear relationship with the applied stress.

This divergence is of principal importance, as the difference between the total and elastic strain curves provides a direct, quantitative measurement of the evolving plastic strain component $\varepsilon^p = \varepsilon - \varepsilon^e$. The ability to experimentally decouple the strain components in real-time forms the foundation of the methodology presented in this work.

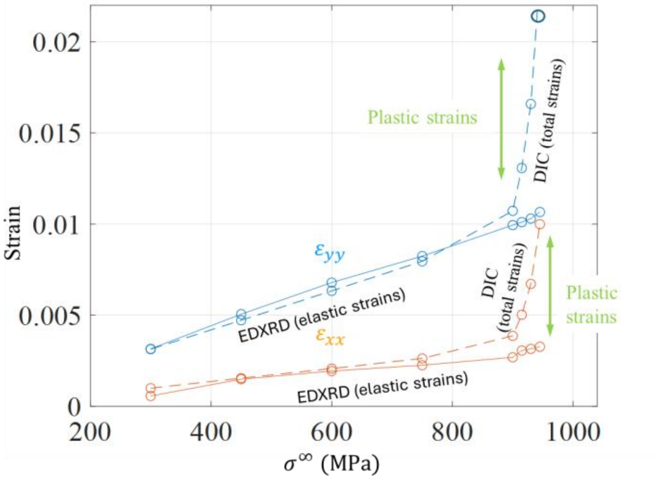

Figure 6 Direct experimental decomposition of strain from a uniaxial tensile test, plotting strain components versus applied stress. The total axial (ϵyy, blue dashed line) and transverse (ϵxx, orange dashed line) strains measured by DIC are compared with the corresponding elastic strains measured by EDXRD (solid lines). The excellent agreement between the total and elastic components in the initial elastic region serves as a cross-validation of the techniques. The divergence of the curves upon yielding allows for the direct measurement of the evolving plastic strain as the difference between the total and elastic measurements.

5.2 Determination of Elastic Constants:

Building on the direct comparison of strain measurements, the data from the uniaxial test was further leveraged to determine the material's elastic constants, providing a quantitative validation of the methodology. At each discrete increment of the stepwise loading protocol, Young's Modulus (E) and Poisson's ratio (ν) were calculated. Specifically, the secant Young's Modulus was computed as the ratio of the global applied stress to the axial strain as in equation 5 below, and Poisson's ratio was computed as the negative ratio of the transverse to the axial strain as in equation 6.

$$\mathrm{E}=\frac{\sigma^{\infty}}{\varepsilon_{yy}} \qquad \text{Eq 5}$$

$$\nu=-\frac{\varepsilon_{xx}}{\varepsilon_{yy}} \qquad \text{Eq 6}$$

This was performed independently using both the elastic strain tensor from the EDXRD measurements and the total strain tensor from the DIC measurements. The latter calculation yields an 'apparent' constant, influenced by plastic deformation.

The evolution of these calculated elastic constants as a function of the applied axial strain is presented in Figure 7.

In this figure, values for Young's Modulus are plotted in black, and values for Poisson's Ratio are plotted in blue. The results derived from the EDXRD data (elastic strain) are shown with solid lines, while those derived from the DIC data (total strain) are represented by dashed lines.

The results provide two key insights. Firstly, within the elastic regime, the constants derived from both measurement techniques show good agreement, yielding stable and consistent values. Secondly, upon the onset of plasticity, a clear divergence is observed. The apparent constants calculated from the DIC data deviate significantly as the total strain measurement becomes increasingly dominated by plastic flow. In contrast, the true elastic constants, derived from the EDXRD lattice strains, remain consistent throughout the entire test, even deep into the plastic regime. This demonstrates the method's powerful capability to isolate and measure true elastic properties regardless of the material's plastic state.

The numerical values extracted from the linear elastic portion of the EDXRD data for the Ti-6Al-4V specimen were E = 115±3.5 GPa and ν = 0.35±0.012. A detailed justification for these uncertainty intervals is provided in the Uncertainty Quantification section. These values are in excellent agreement with the accepted specifications for this alloy, providing strong confidence in the accuracy of the entire experimental and analytical framework.

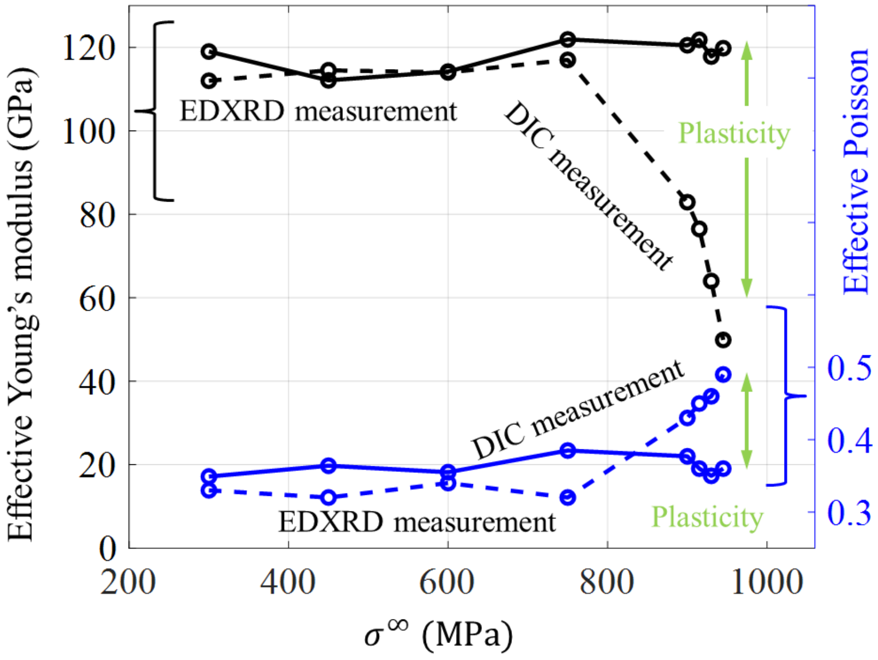

*Figure 7 Graph shows the evolution of **Young's Modulus** (black) and **Poisson's ratio** (blue) as a function of the applied load. The **true elastic constants**, derived from EDXRD data (**solid lines**), remain stable throughout the entire test. In contrast, the 'apparent' constants, calculated from the DIC total strain data (**dashed lines**), deviate significantly after the onset of plasticity. This result validates the accuracy of the XRD-based measurement for determining elastic properties, even in the presence of plastic deformation*

5.3 Verification of Uniaxial Load State via In-situ Specimen Rotation:

To experimentally verify the uniaxial nature of the applied load and quantify any potential parasitic shear strains, a procedure analogous to a strain gauge rosette analysis was performed on a uniaxial "dog-bone" specimen. This involved measuring two orthogonal components of strain ($\varepsilon_{xx}\ and\ \varepsilon_{yy}$) at two different orientations in the plane of the specimen. Thus, we have four measurements of strain along four different directions while only three measurements are required to obtain the in-plane strain tensor at a point. The four-step measurement protocol is illustrated schematically in Figure 8. As depicted in Figure 8(A), the procedure began with characterizing the pristine (unloaded) specimen to establish a stress-free reference state. This was done at two orientations: first, with the specimen physically rotated to 17.5° (Step ①), and subsequently at the nominal 0° orientation (Step ②). Following this, a static tensile load was applied and held constant. As illustrated in Figure 8(B), the measurement sequence was then repeated on the loaded specimen, first at the 0° orientation (Step ③) and finally at the 17.5° orientation (Step ④). The lattice strain for each loaded orientation (Steps ③ and ④) was calculated relative to the pristine reference measurement taken at the corresponding angle (Steps ② and ①, respectively). The normal strains measured at 0° and 17.5° were then used in a strain-transformation analysis (Hibbeler, 2022) to determine the full in-plane strain tensor. A Mohr's circle analysis was subsequently performed on the resulting strain tensor to find the orientation of the major principal strain axis θ_p. The analysis yielded a principal strain angle of 1.4°. This near-zero value falls well within our previously established measurement uncertainty and provides strong experimental evidence that the loading state is purely uniaxial with negligible shear. Furthermore, this successful validation demonstrates that the rotation protocol can be used to measure the full in-plane strain tensor, by constructing the Mohr circle or by applying the standard strain-transformation equations.

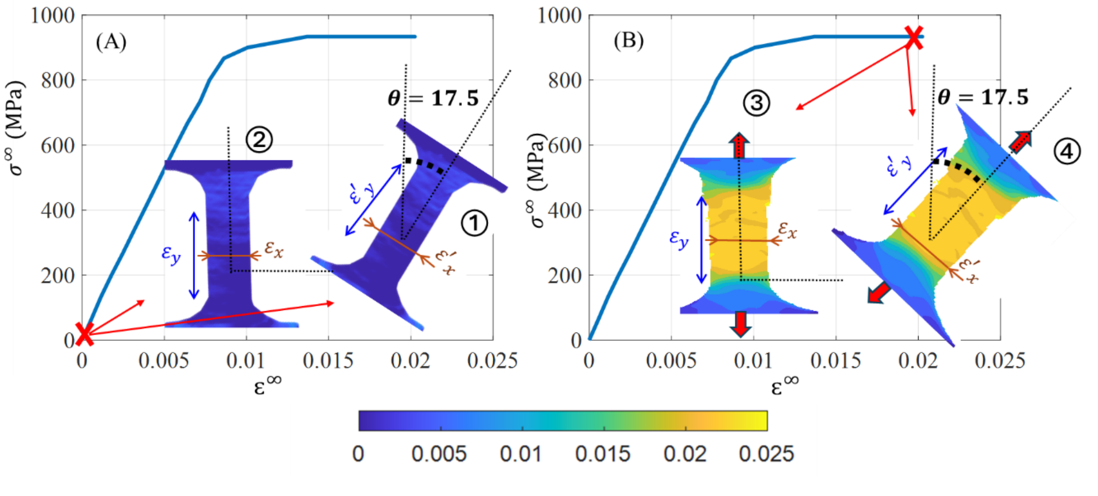

Figure 8: A schematic of the four-step protocol used to verify the uniaxial load state. (A) The pristine (unloaded) specimen is measured at two orientations, 17.5° (Step ①) and 0° (Step ②), to establish a stress-free reference. (B) The sequence is repeated under a static tensile load, with measurements again taken at 0° (Step ③) and 17.5° (Step ④).This process provides the data needed for a Mohr's circle analysis to confirm that parasitic shear strains are negligible.

5.4 Notch specimen- Global Force Equilibrium

Following the comprehensive validation of the experimental technique, the combined DIC-EDXRD methodology was applied to a statically indeterminate (semi-circular notch) specimen. To visualize the continuous strain fields from the discrete pointwise measurements, the experimental data were spatially interpolated onto a regular 2D grid. This was performed using a linear interpolation algorithm, ensuring that the visualized maps faithfully represent the measured values without introducing artificial smoothing. The predicted elastic axial strain (ε_{yy}^{e}), field for this geometry at a global force of 2500 N, as determined by the previously described FE analysis, is shown for reference in Figure 9 (A).

To experimentally capture this strain distribution, a comprehensive validation scan consisting of 61 discrete measurement points was first performed across the entire region of interest. The resulting experimental map of the elastic axial strain, also at a global force of 2500 N, is presented in Figure 9 (B). A key observation from this full dataset is the high degree of symmetry exhibited by the strain field about both the horizontal and vertical centrelines.

This observed symmetry validates the use of a more time-efficient, expedited scanning protocol. For this protocol, only 20 measurement points were acquired in a single quadrant of the specimen, and the full-field map was then reconstructed by Mirroring the measurement grid across the symmetry axes, as shown in Figure 9 (C). Given the excellent agreement between the full Figure (9B) and reconstructed Figure 9(C) maps, and the critical need to minimize data acquisition time to mitigate stress relaxation effects, this expedited 20-point protocol was adopted for all subsequent multi-step loading experiments.

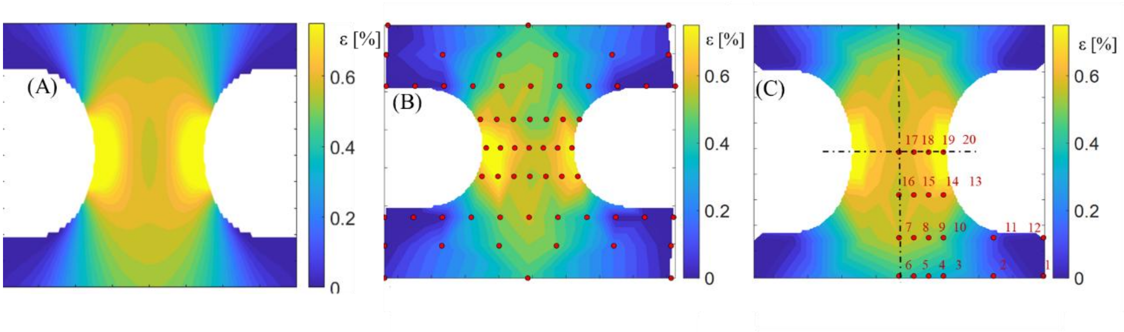

Figure 9 A comparison of the elastic axial strain (ε_{yy}^{e}) maps in the notched specimen, measured at a constant global force of 2500 N.(A) FE analysis.(B) Strain field obtained from a comprehensive 61-point scan. (C) Strain field reconstructed from an expedited 20-point scan by applying symmetry. The strong qualitative agreement between the two maps validates the use of the faster, 20-point protocol for subsequent measurements, which minimizes the effects of stress relaxation

The validated dual-measurement methodology was employed to investigate the strain evolution in the notched Ti-6Al-4V specimen under a stepwise loading protocol. Figure 10 shows the global load-displacement curve for this test. The displacement, plotted as a red line, was calculated from the DIC data by tracking the relative movement of the regions nearest the loading grips. The blue asterisks on the curve mark the discrete points at which the loading was paused for the full-field EDXRD and DIC data acquisition, illustrating the elastic, plastic, and final unloading phases of the experiment.

The full-field strain maps at two critical states—peak load (3500 N) and after complete unloading (0 N)—are presented for both the axial (ε_{yy}) and transverse (ε_{xx}) components in Figure 11 and Figure 12, respectively. In these figures, the left panels show the total strain fields measured by DIC, while the right panels show the corresponding elastic strain fields measured by EDXRD.

At the peak applied force of 3500 N (top panels of Figure 11 and Figure 12), both techniques clearly capture the expected strain concentration at the notch root. However, a quantitative analysis reveals a significant disparity between the total and elastic strain magnitudes. Along the notch centreline, the maximum total axial strain (ε_{yy}) measured by DIC reached 4.8%. In contrast, the corresponding elastic strain from XRD was only 0.94%. This large difference underscores the significant amount of plastic flow at the notch root, where the total deformation is more than five times its elastic component. A similar trend is observed in the transverse direction (ε_{xx}), where the total strain was -1.2% (DIC) versus an elastic component of -0.18% (EDXRD).

The analysis of the specimen after unloading to 0 N provides the most powerful demonstration of the technique's capability. As shown in the bottom-right panels of Figure 11 and Figure 12, the elastic strain field measured by XRD has returned to a near-zero, stress-free state, with residual elastic strains of only 0.04% in the axial direction and -0.06% in the transverse direction.

In stark contrast, the DIC measurement (bottom-left panels) reveals a significant residual strain field, which directly visualizes the permanent plastic deformation remaining in the specimen. The residual axial and transverse strains at the notch root were measured to be 4.5% and -1.1%, respectively. By subtracting the negligible residual elastic field (EDXRD) from the total residual field (DIC), this methodology provides a direct and experimentally robust measurement of the plastic strain field (ε^{p}), a critical parameter for the development and validation of advanced plasticity models.

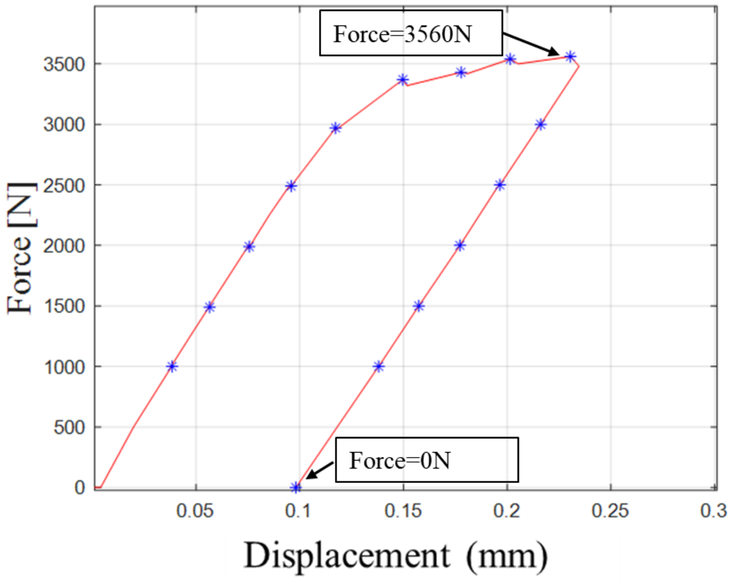

Figure 10 Force - displacement curve for notch specimen, EDXRD measurement points are indicated by the asterisk (*) symbol. At these load points the sample was held under displacement control while EDXRD patterns were collected at a series of spatial location on the specimen.

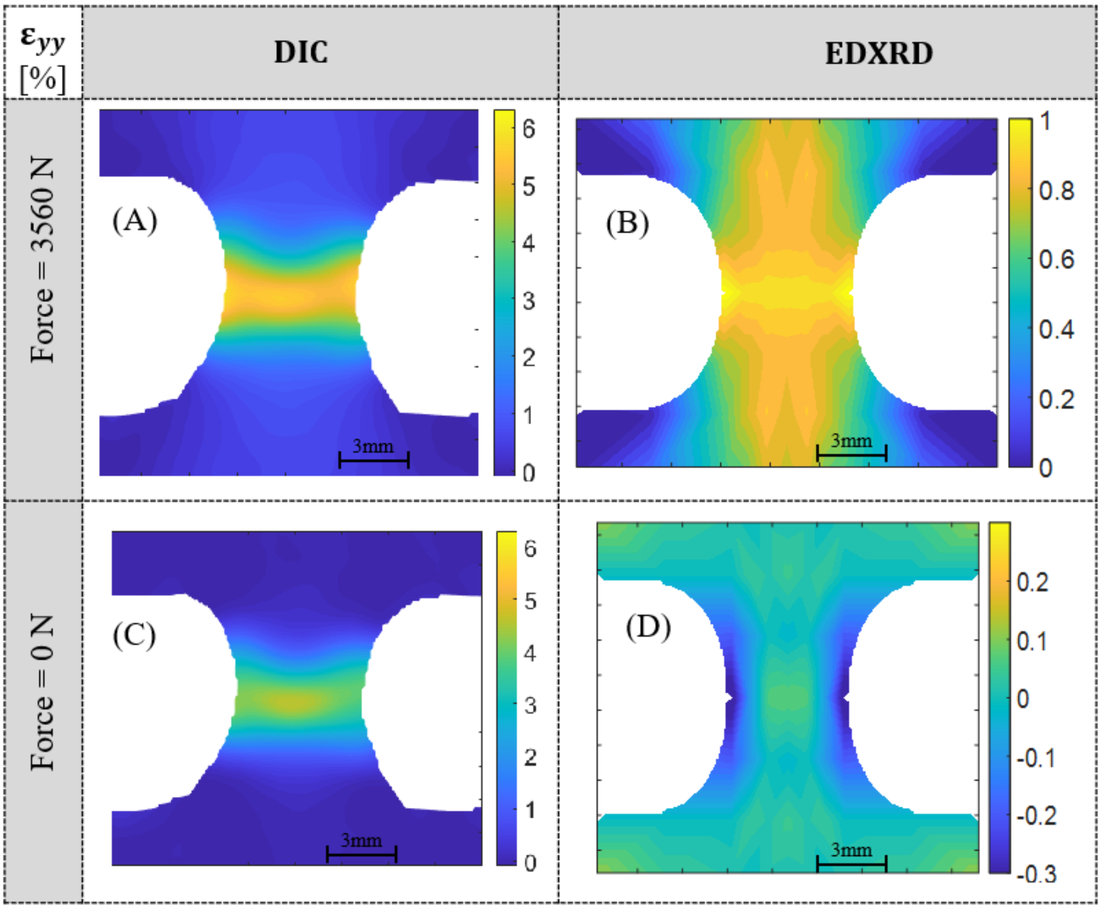

*Figure 11 Full-field axial strain (εyy) distribution in the notched specimen at peak load and after unloading.**(A)** The total strain field as measured by DIC at the peak applied load (3500 N).**(B)** The corresponding elastic strain field measured by EDXRD at peak load.**(C)** The residual total strain field from DIC after the specimen has been*

completely unloaded, directly visualizing the permanent plastic deformation. ***(D)*** *The residual elastic strain field from EDXRD after unloading, showing a near-zero, stress-free state.The direct comparison between the total (DIC) and elastic (EDXRD) fields allows for a quantitative, full-field decomposition of the plastic strain.*

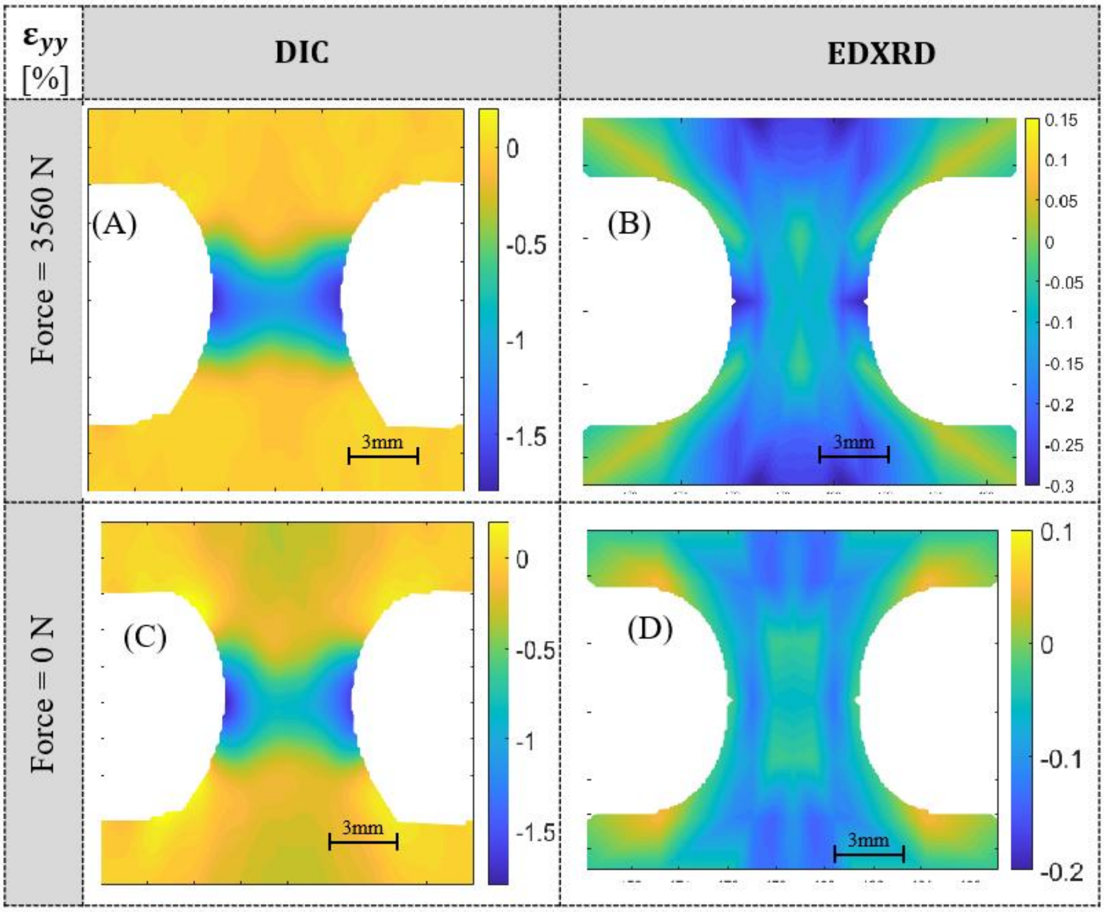

Figure 12 Full-field axial strain (εxx) distribution in the notched specimen at peak load and after unloading. ***(A)*** *The total strain field as measured by DIC at the peak applied load (3500 N).* ***(B)*** *The corresponding elastic strain field measured by EDXRD at peak load.* ***(C)*** *The residual total strain field from DIC after the specimen has been completely unloaded, directly visualizing the permanent plastic deformation.* ***(D)*** *The residual elastic strain field from EDXRD after unloading, showing a near-zero, stress-free state.The direct comparison between the total (DIC) and elastic (EDXRD) fields allows for a quantitative, full-field decomposition of the plastic strain*

For each load step of the experiment, the axial (σ_{yy}) and transverse (σ_{xx}) stress components were calculated at every point in the measurement grid by applying isotropic Hooke's Law to the measured elastic strain components, ε_{yy}^{e} and ε_{xx}^{e}.

Figure 13 presents the resulting stress contour maps for the two principal stress components at two representative states: peak load (3500 N) and after complete unloading. The top panels show the stress distribution at maximum force, while the bottom panels show the residual stress state after unloading.

A final, powerful validation of the computed stress field was performed by applying the principle of force equilibrium. The internal force acting across the specimen's net cross-section was calculated by integrating the computed axial stress field (σ_{yy}) along the paths indicated by the red lines in Figure 13-top left. This integrated internal force was then compared to the externally applied force measured by the system load cell (3500 N).

This comparison showed excellent agreement, with a maximum deviation of less than 5% between the experimentally calculated internal force and the externally measured load. This successful validation provides high confidence in the accuracy of the computed stress fields at all measured load steps.

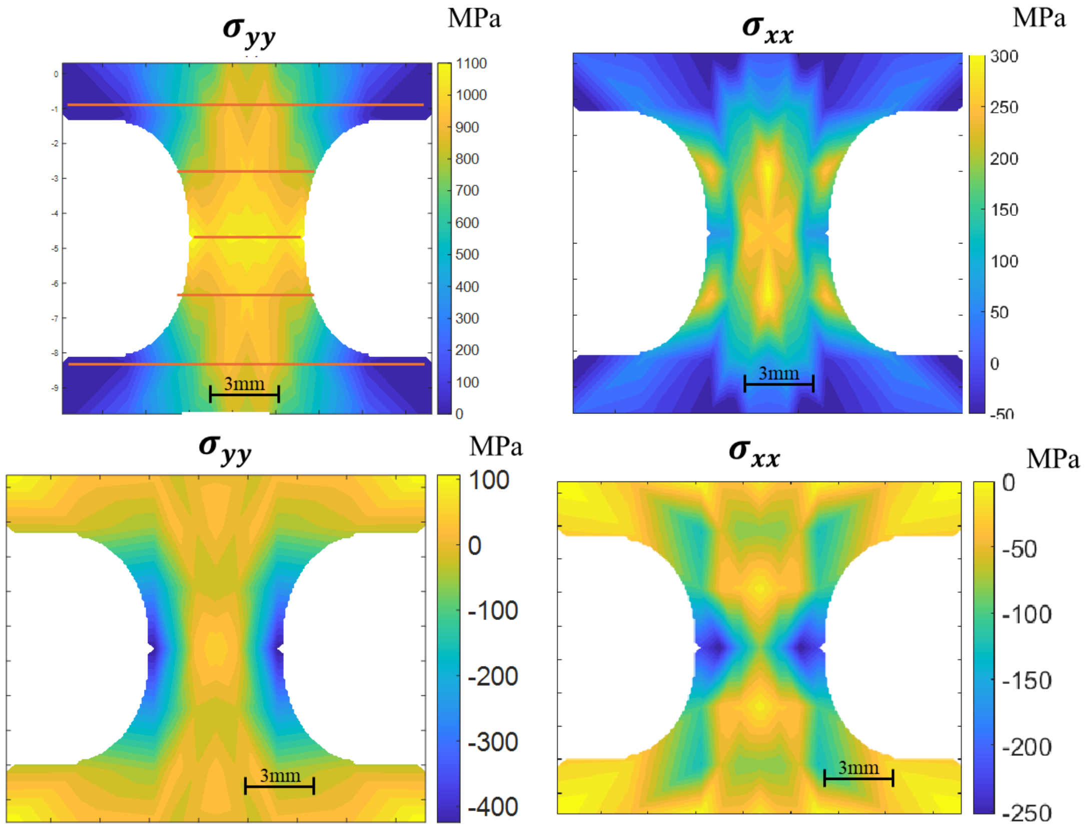

Figure 13 Computed stress fields in the notched specimen, derived from the experimental elastic strain data. The top panels show the axial (σ yy) and transverse (σ xx) stress at peak load (3500 N), while the bottom panels show the residual stress state after unloading.The red lines in the top-left panel indicate the integration path used for a force equilibrium check. The internal force calculated from this stress field matched the externally measured load to within 5%, validating the accuracy of the computed stress maps.

5.5 Full-Field Analysis on a Notched Specimen

A key advantage of the combined full-field measurement technique is the ability to extract the local stress-strain response at any point within the measured grid. This allows for a detailed, spatially-resolved analysis of the material's constitutive behavior. The local stress tensor at each point was taken from the EDXRD-derived stress field, while the corresponding local strain tensor was taken from the DIC-measured total strain field.

To illustrate this capability, Figure 14 presents the local stress-strain curves for three representative points 8,13, and 18—whose spatial locations across the notch are shown in Figure 9. The left panel of the graph displays the axial stress-strain response (σ_{yy} vs ε_{yy}), while the right panel displays the transverse response (σ_{xx} vs ε_{xx}).

The results clearly demonstrate the heterogeneous nature of the deformation. Point 8, located far from the stress concentrator, exhibits a purely linear and elastic response, serving as a baseline for the material's intrinsic behavior. Moving closer, point 13 shows a distinct yield point and the onset of plasticity. Finally, point 18, situated at the notch root where deformation is most severe, displays significant plastic flow and strain hardening. As expected, the magnitude of the strain and the degree of plasticity are significantly more pronounced in the axial (YY) direction than in the transverse (XX) direction.

The richness of this dataset is a primary strength of the methodology. While only three points are shown for clarity, such constitutive curves can be extracted for every measured point. Furthermore, through spatial interpolation of the stress and strain fields between these points, it is possible to generate a continuous, high-resolution map of the local material response. This ability to capture a wide spectrum of behaviors, from pure elasticity to extensive plasticity, all within a single test, provides an unprecedented level of data for understanding and modeling material behavior under complex loading.

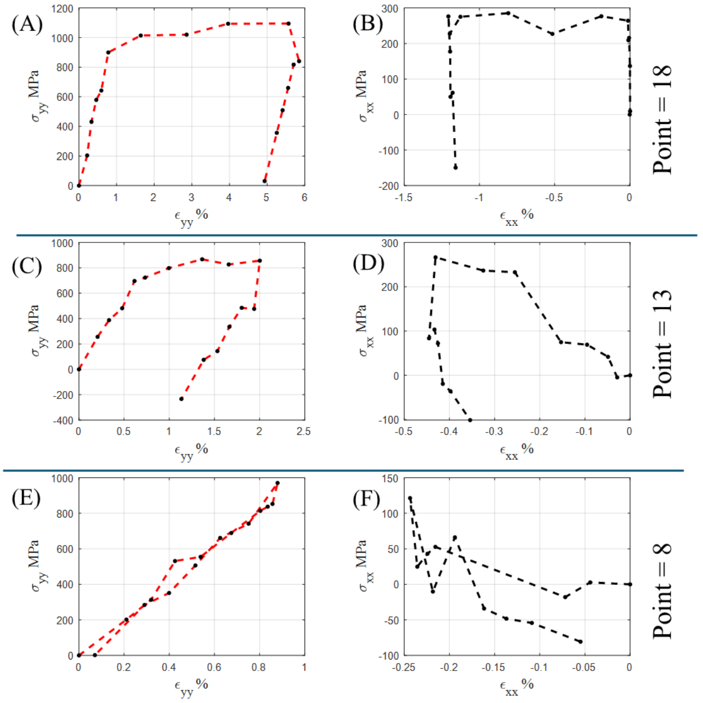

Figure 14 : Local stress-strain curves for three representative points (8, 13, and 18) in the notched specimen. The spatial locations of these points are shown in Figure 8. The left panel, figures A,C snd E, shows the axial response (σ_{xx} vs ε_{xx}), and the right panel , figures B,D snd F shows the transverse response (σ_{yy} vs ε_{yy}). The graph highlights the heterogeneous material behavior at different locations, from nearly elastic (Point 8) to highly plastic (Point 18).

Local Stress-Strain Measurements $\sigma_{yy}\ vs\ \varepsilon_{yy}$

To assess the predictive capability of the standard constitutive model, the experimental results were directly compared against the predictions from the previously described FE analysis. As detailed in Section 4.3, the simulation employs a classical J2 plasticity model with isotropic hardening, calibrated using the macroscopic true stress-strain data from the uniaxial "dog-bone" specimen test. It is therefore important to recall that this standard calibration procedure is inherently associated with the material's response in the primary loading (YY) direction.

For a detailed, local comparison, three representative locations were selected from the notched specimen, as shown in Figure 8: Point 17: Located on the specimen's centerline, far from the notch. Point 20: Located on the centerline but at the root of the notch, experiencing the highest strain. Point 13: An off-axis point, subjected to a complex, multiaxial stress state with a significant shear component.

Figure 15 presents a direct comparison of the experimentally measured stress-strain curves and the predictions from the J2 plasticity model at these three locations. The figures on the left hand side (A,C and E) show the axial response $\sigma_{yy}\ vs\ \varepsilon_{yy}$, and the figures on the right hand side (B,D and F) show the transverse response $\sigma_{xx}\ vs\ \varepsilon_{xx}$.

The results in the axial (YY) direction, shown in the top panels, indicate that the J2 model provides a reasonably good prediction of the material's behavior at all three points. This is largely expected, as the model was calibrated using the material's response in this primary direction.

However, a significant discrepancy between the model and the experiment becomes evident in the transverse (XX) direction, as shown in the bottom panels. For points 17 and 20 on the symmetry line, the model's prediction of the transverse response is already poor. This discrepancy becomes even more pronounced for Point 13, which is located in the off-axis, high-shear region.

This highlights a critical limitation of the standard modelling approach: while the J2 model can adequately replicate the primary response it was calibrated with, its ability to predict the full, multiaxial stress-strain behaviour is severely limited. The model's failure is exacerbated by the presence of shear and non-proportional loading paths, which are not captured in a simple uniaxial calibration test. These findings underscore the necessity of advanced, full-field experimental techniques, such as the one presented here, for the rigorous validation and future development of constitutive models for complex engineering applications.

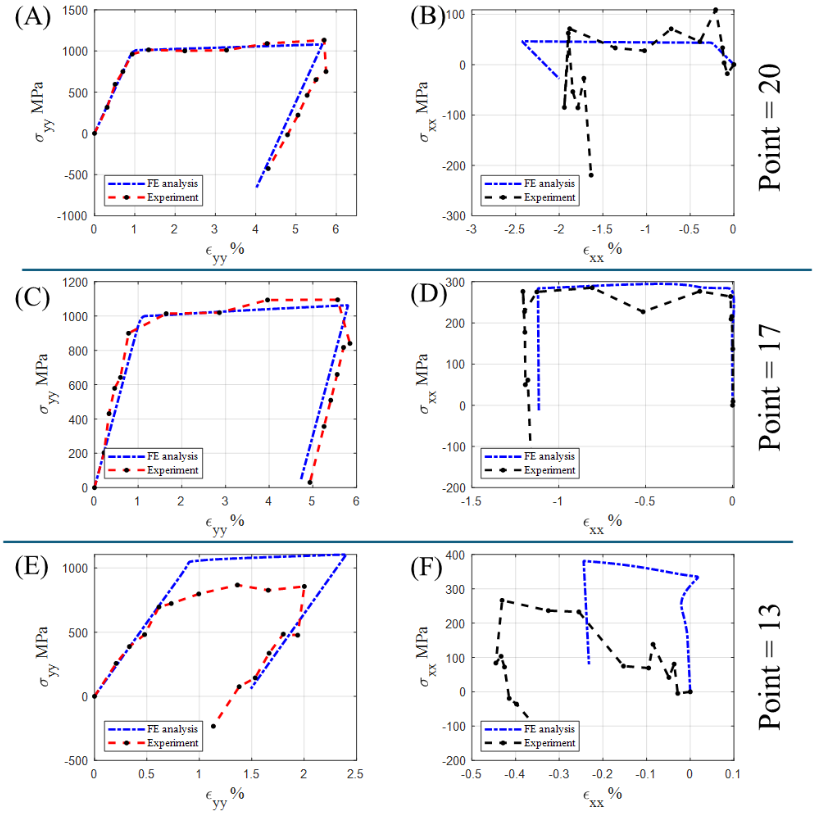

Figure 15 A local comparison between the ***experimental*** *stress-strain curves (solid lines) and the predictions from the* ***J2 plasticity model*** *(dashed lines) at three representative locations in the notched specimen.The* ***top panels*** *show the axial response (* $\sigma_{yy} vs\ \varepsilon_{yy}$*,), and the* ***bottom panels*** *show the transverse response (*$\sigma_{xx} vs\ \varepsilon_{xx}$*). The comparison highlights the model's reasonable accuracy in the loading direction (top) and its significant deviation in the transverse direction (bottom), particularly at the off-axis location subjected to shear.*

5.6 Uncertainty Quantification

Uncertainty Quantification

The local stress-strain curves presented in the previous section are subject to measurement uncertainty. This section details the methodology used to quantify this uncertainty. The two normal stresses are computed from their corresponding measured strain components using the elastic constants E, μ via the isotropic Hooke's Law.

$$\sigma_{yy} = \frac{E}{1-\mu^2}\left[\varepsilon_{yy}^{e} + \mu\varepsilon_{xx}^{e}\right]$$

$$\sigma_{xx} = \frac{E}{1-\mu^2}\left[\varepsilon_{xx}^{e} + \mu\varepsilon_{yy}^{e}\right]$$

Therefore, the uncertainty (S) in the calculated stress is a function of the uncertainties in each of these input parameters.

$$S\sigma = f(S\varepsilon_{xx}, S\varepsilon_{yy})$$

Uncertainty in Elastic Constants

The elastic constants were treated as fixed parameters in the final uncertainty propagation, based on their low variance as determined from a series of five independent uniaxial tensile tests (data presented in Figure 5).

Young's Modulus (E): For each test, was determined from a linear regression of the elastic stress-strain data. A null hypothesis test on the fit yielded a p-value of less than 3.5x10^{-3} in all cases, confirming a strong linear relationship. The standard deviation of the modulus across the five tests was 17.5 MPa. For the stress calculation, the average value of E = 105 GPa was used as a constant.

Poisson's Ratio (ν): Poisson's ratio was calculated from the DIC data in the elastic regime

$$-\frac{\varepsilon_{xx}}{\varepsilon_{yy}}$$

for the same five tests. The average value was found to be μ= 0.33 with a standard deviation of 0.009. This value was also treated as a constant.

Uncertainty in Elastic Strain Measurement

The primary source of uncertainty in the stress calculation stems from the measurement of the elastic strain components (ε_{xx}^{e} and ε_{yy}^{e}). This uncertainty was quantified using the pristine (unloaded) scan of the notched specimen. In this state, the strain field is assumed to be uniform and zero. Therefore, the statistical variation of the measured diffraction peak energies across all measurement points provides a direct measure of the baseline experimental uncertainty.

A Lilliefors (Lilliefors, 1967) test performed on data from the uniaxial specimen confirmed that the measurement errors for both strain components follow a normal distribution, justifying the use of the standard deviation as a robust uncertainty metric. For the notched specimen, the data acquisition time was set to ensure that the maximum standard deviation of the measured peak energies in the pristine state did not exceed 10 eV. This energy variance was used as a conservative upper bound for the measurement uncertainty, which translates to a strain uncertainty of ~ 2.8 x 10^{-4}

Propagation of Uncertainty to Stress

The uncertainty in the calculated stress components was determined using the standard formula for propagation of uncertainty(Taylor, 2022).

$$s_{\sigma}^{2} = \left(\frac{\partial f}{\partial \varepsilon_{xx}}\right)^{2} s_{\varepsilon_{xx}}^{2} + \left(\frac{\partial f}{\partial \varepsilon_{yy}}\right)^{2} s_{\varepsilon_{yy}}^{2}$$

Given that E and μ were treated as constants with negligible variance, the uncertainty in stress is dominated by the uncertainty in the measured strains. The propagated uncertainties for the axial $S\sigma_{yy}$ and transverse $S\sigma_{xx}$ stress components were thus calculated to be ±33.4 MPa and ±34.2 MPa, respectively.

DIC Measurements

The uncertainty of the full-field strain measurements obtained via DIC was determined experimentally for the specific in-situ setup. To quantify the strain resolution, a zero-strain test was conducted by inducing a rigid body motion.

Prior to the application of mechanical load, a set of images of the stationary specimen was acquired. Subsequently, the specimen was subjected to a rigid body translation and rotation, with a magnitude comparable to the displacements observed during the actual experiment. A second set of images was then captured in this new position.

This image set was processed using the DIC software Vic-3D to compute the resulting strain field. Since a rigid body motion should theoretically induce zero strain, any non-zero values in the computed strain field can be attributed to the measurement noise floor, which incorporates all sources of error including camera sensor noise, lighting variations, and speckle pattern quality. The strain measurement uncertainty was then quantified as the standard deviation of this artificial strain field. For the presented results, the strain resolution was determined to be approximately 50 $\mu\epsilon$. This was achieved using a subset size of 35x35 pixels and a step size of 7 pixels.

6 Conclusions and Outlook

In this work, we have presented the design, development, and validation of a novel, laboratory-based experimental methodology that combines EDXRD with DIC. This system provides a powerful new capability for the simultaneous, full-field measurement of both elastic and total strain fields in metallic components. We have successfully demonstrated its accuracy through a series of validation tests and applied it to reveal the complex, heterogeneous strain and stress distributions in a notched specimen under load.

The primary conclusion of this study is that this laboratory-based technique successfully provides the high-fidelity, stress-strain pairs necessary to calibrate continuum-scale constitutive models. Our direct comparison revealed that a standard J2 plasticity model, calibrated from conventional uniaxial data, fails to capture the true multiaxial stress state, particularly in the transverse direction and in off-axis regions subjected to shear.

The broader significance of this work lies in the accessibility of an advanced characterization capability that was, until recently, exclusive to limited-access synchrotron facilities. This transition to a laboratory environment fundamentally accelerates the calibration and validation of constitutive models for crystalline materials. A single experiment on a complex-geometry specimen can now provide a rich dataset of diverse stress paths, replacing the need for numerous, time-consuming tests on different specimen geometries.

Furthermore, by moving this technique from a time-limited user facility to the local laboratory, our methodology unlocks the potential for long-duration in-situ experiments, such as fatigue, creep, and stress-corrosion studies, which are impractical to perform at synchrotrons. Finally, the high-fidelity, full-field experimental data generated by this method provides an ideal and essential foundation for the development and training of the next generation of data-driven and machine learning-based material models.

References

Bulavchenko, O. A., & Vinokurov, Z. S. (2023). In Situ X-ray Diffraction as a Basic Tool to Study Oxide and Metal Oxide Catalysts. *Catalysts*, *13*(11), 1421. https://doi.org/10.3390/catal13111421

Chen, Y., Wang, X., Song, Q., Xu, J., & Mu, B. (2018). Development of a high-energy-resolution EDXRD system with a CdTe detector for security inspection. *AIP Advances*, *8*(10). https://doi.org/10.1063/1.5052027

Croft, M., Jisrawi, N., Zhong, Z., Horvath, K., Holtz, R. L., Shepard, M., Lakshmipathy, M., Sadananda, K., Skaritka, J., Shukla, V., Sadangi, R. K., & Tsakalakos, T. (2008). Stress Gradient Induced Strain Localization in Metals: High Resolution Strain Cross Sectioning via Synchrotron X-Ray Diffraction. *Journal of Engineering Materials and Technology*, *130*(2). https://doi.org/10.1115/1.2840962

Daymond, M. R. (2004). The determination of a continuum mechanics equivalent elastic strain from the analysis of multiple diffraction peaks. *Journal of Applied Physics*, *96*(8), 4263–4272. https://doi.org/10.1063/1.1794896

Greenberg, J., & Iniewski, K. (Eds.). (2018). *X-Ray Diffraction Imaging*. CRC Press. https://doi.org/10.1201/9780429196492

Hemley, R. J., Mao, H., & Struzhkin, V. V. (2005). Synchrotron radiation and high pressure: new light on materials under extreme conditions. *Journal of Synchrotron Radiation*, *12*(2), 135–154. https://doi.org/10.1107/S0909049504034417

Hibbeler, R. C. . (2022). *Mechanics of materials*. Pearson Education Inc.

Jeffries, C. M., Ilavsky, J., Martel, A., Hinrichs, S., Meyer, A., Pedersen, J. S., Sokolova, A. V., & Svergun, D. I. (2021). Small-angle X-ray and neutron scattering. *Nature Reviews Methods Primers*, *1*(1), 70. https://doi.org/10.1038/s43586-021-00064-9

Lilliefors, H. W. (1967). On the Kolmogorov-Smirnov Test for Normality with Mean and Variance Unknown. *Journal of the American Statistical Association*, *62*(318), 399–402. https://doi.org/10.1080/01621459.1967.10482916

Ludwig, W., Reischig, P., King, A., Herbig, M., Lauridsen, E. M., Johnson, G., Marrow, T. J., & Buffière, J. Y. (2009). Three-dimensional grain mapping by x-ray diffraction contrast tomography and the use of Friedel pairs in diffraction data analysis. *Review of Scientific Instruments*, *80*(3). https://doi.org/10.1063/1.3100200

Mäde, K., Reisgen, U., Sharma, R., Akyel, F., Olschok, S., Gamerdinger, M., Evers, T., Krishna Murthy, K. R., Olesch, M., Kellerwessel, J., Faria, G. A., & Dovzhenko, G. (2024). Synchrotron EDXRD strain-temperature measurement during laser welding. *Proceedings of the Institution of Mechanical Engineers, Part L: Journal of Materials: Design and Applications*, *238*(12), 2406–2412. https://doi.org/10.1177/14644207241249765

Mino, L., Borfecchia, E., Segura-Ruiz, J., Giannini, C., Martinez-Criado, G., & Lamberti, C. (2018). Materials characterization by synchrotron x-ray microprobes and nanoprobes. *Reviews of Modern Physics*, *90*(2), 025007. https://doi.org/10.1103/RevModPhys.90.025007

Oh, S., Jin, Y., Lee, S., Li, W., Geauvreau, K., Williams, M., Drake, R., & Bucsek, A. (2025). Taking three-dimensional x-ray diffraction (3DXRD) from the synchrotron to the laboratory scale. *Nature Communications*, *16*(1), 3964. https://doi.org/10.1038/s41467-025-58255-x

Permann, C. J., Gaston, D. R., Andrš, D., Carlsen, R. W., Kong, F., Lindsay, A. D., Miller, J. M., Peterson, J. W., Slaughter, A. E., Stogner, R. H., & Martineau, R. C. (2020). MOOSE: Enabling massively parallel multiphysics simulation. *SoftwareX*, *11*, 100430. https://doi.org/10.1016/j.softx.2020.100430

Poulsen, H. F., Nielsen, S. F., Lauridsen, E. M., Schmidt, S., Suter, R. M., Lienert, U., Margulies, L., Lorentzen, T., & Juul Jensen, D. (2001). Three-dimensional maps of grain boundaries and the stress state of individual grains in polycrystals and powders. *Journal of Applied Crystallography*, *34*(6), 751–756. https://doi.org/10.1107/S0021889801014273

Shishvan, S. S., & Deshpande, V. S. (2025). Evaluation of the ability of full-field displacement measurements to extract yield surface parameters. *European Journal of Mechanics - A/Solids*, *112*, 105652. https://doi.org/10.1016/j.euromechsol.2025.105652

Stan, C., Beavers, C., Kunz, M., & Tamura, N. (2018). X-Ray Diffraction under Extreme Conditions at the Advanced Light Source. *Quantum Beam Science*, *2*(1), 4. https://doi.org/10.3390/qubs2010004

Stuhrmann, H. B. (1989). Small-angle scattering of X-rays. *Progress in Crystal Growth and Characterization*, *18*, 1–19. https://doi.org/10.1016/0146-3535(89)90023-3

Taylor, J. R. . (2022). *An introduction to error analysis : the study of uncertainties in physical measurements*. University Science Books.

Withers, P. J., & Bhadeshia, H. K. D. H. (2001). Residual stress. Part 1 – Measurement techniques. *Materials Science and Technology*, *17*(4), 355–365. https://doi.org/10.1179/026708301101509980

Zhang, W., Simpson, C. A., Lopez-Crespo, P., Mokhtarishirazabad, M., Buslaps, T., Pippan, R., & Withers, P. J. (2020). The effect of grain size on the fatigue overload behaviour of nickel. *Materials & Design*, *189*, 108526. https://doi.org/10.1016/j.matdes.2020.108526